Physics in Medicine & Biology

PAPER • OPEN ACCESS

Low activity [^{11}C]raclopride kinetic modeling in the mouse brain using the spatiotemporal kernel method

To cite this article: Alan Miranda *et al* 2021 *Phys. Med. Biol.* **66** 115005

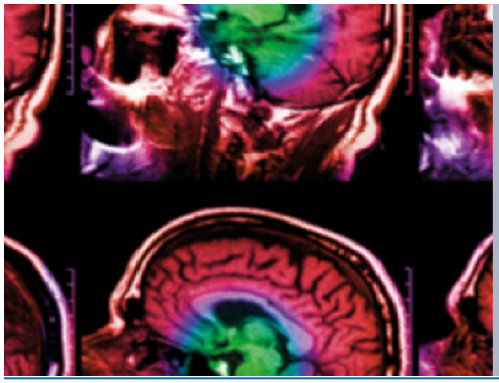

Physics in Medicine & Biology

IPEM Institute of Physics and Engineering in Medicine

OPEN ACCESS

RECEIVED
4 January 2021

REVISED
11 April 2021

ACCEPTED FOR PUBLICATION
27 April 2021

PUBLISHED
20 May 2021

PAPER

Low activity [^{11}C]raclopride kinetic modeling in the mouse brain using the spatiotemporal kernel method

Alan Miranda[1,*], **Daniele Bertoglio**[1], **Sigrid Stroobants**[1,2], **Steven Staelens**[1] and **Jeroen Verhaeghe**[1]

[1] Molecular Imaging Center Antwerp, University of Antwerp, Universiteitsplein 1, B-2610 Antwerp, Belgium
[2] University Hospital Antwerp, Wilrijkstraat 10, B-2650 Antwerp, Belgium
[*] Author to whom any correspondence should be addressed.

E-mail: alan.mirandamenchaca@uantwerpen.be, daniele.bertoglio@uantwerpen.be, sigrid.stroobants@uza.be, steven.staelens@uantwerpen.be and jeroen.verhaeghe@uantwerpen.be

Keywords: PET, kinetic modeling, mouse brain

Supplementary material for this article is available online

Abstract

Depending on the molar activity of the tracer, the maximal allowable injected activity in mouse brain PET studies can be extremely low in order to avoid receptor saturation. Therefore, a high level of noise can be present in the image. We investigate several dynamic PET reconstruction methods in reduced counts, or equivalently in reduced injected activity, data exemplified in [^{11}C]raclopride BP_{ND} and R_1 quantification using the simplified reference tissue model (SRTM). We compared independent frame reconstruction (IFR), post-reconstruction HYPR denoising (IFR + HYPR), direct reconstruction using the SRTM model (DIR-SRTM), and the spatial (KERS) and spatiotemporal kernel reconstruction (KERST). Additionally, HYPR denoising of the frames used as features for the calculation of the spatial kernel matrix, was investigated (KERS-HYPR and KERST-HYPR). *In vivo* data of 11 mice, was used to generate list-mode data for five reduced count levels corresponding to reductions by a factor 4, 8, 12, 16 and 32 (equivalently 2.07, 1.04, 0.691, 0.518, and 0.260 MBq). Correlation of regional BP_{ND} and R_1 values (reduced versus full counts reconstructions) was high ($r > 0.94$) for all methods, with KERS-HYPR and KERST-HYPR reaching the highest correlation ($r > 0.96$). Among methods with regularization, DIR-SRTM showed the largest variability in BP_{ND} (Bland–Altman SD from 3.0% to 12%), while IFR showed it for R_1 (5.1%–14.6%). KERST and KERST-HYPR were the only methods with Bland–Altman bias and SD below 5% for noise level up to a reduction factor of 16. At the voxel level, BP_{ND} and R_1 correlation was gradually decreased with increasing noise, with the largest correlation (BP_{ND} $r > 0.88$, R_1 $r > 0.62$) for KERS-HYPR and KERST-HYPR. The spatial and the spatiotemporal kernel methods performed similarly, while using only temporal regularization with direct reconstruction showed more variability. Although $R1$ values present noise, using the spatiotemporal kernel reconstruction, accurate estimates of binding potential could be obtained with mouse injected activities as low as 0.26–0.518 MBq. This is desirable in order to maintain the tracer kinetics principle in mouse studies.

1. Introduction

In order to study the living organism without altering its physiological function, tracer (low) concentrations of the radioligand need to be administered to avoid any pharmacological effect. For receptor studies an occupancy of 1% is considered a suitable limit to maintain tracer kinetics (Hume *et al* 1998). This receptor occupancy limit is not only bound to the receptor density (B_{max}), but it also depends on the tracer affinity ($1/K_D$). Considering similar [^{11}C]raclopride affinity ($K_D \approx 1$ nM) across human and rodent species, and a molar activity of 100 MBq/nmol, only 0.3 MBq can be injected in a mouse to keep receptor occupancy below 1% (Hume *et al* 1998).

However, given typical preclinical scanners sensitivities, this activity level can result in reconstruction with high noise.

Quantification in neuronal receptors studies in positron emission tomography (PET) is usually achieved using dynamic imaging and pharmacokinetic modeling to obtain information about neurotransmitter receptor density or the volume of distribution of the tracer (Innis *et al* 2007).

Dynamic PET reconstruction is usually performed by reconstruction of short time (e.g. 10 s) frames in the initial time period of the scan in order to capture the fast initial kinetics of the tracer. Afterwards longer frames can be used for the slower kinetics periods. Since only a fraction of the scan events are used to reconstruct each frame, dynamic frames can present a high level of noise. This noise level can be further exacerbated if tracer activity is limited, severely impacting quantification. For this reason, extensive research has been performed to reduce the noise in dynamic PET reconstruction (Reader and Verhaeghe 2014, Wang *et al* 2020).

One approach to reduce noise in dynamic PET is direct reconstruction (Matthews *et al* 2010). For this method, the kinetic model (either linear or nonlinear) is fitted after every tomographic reconstruction iteration in order to estimate the model parameters for every voxel. This method produces good results when the kinetic model accurately describes the tracer kinetics at every voxel. However, when the model does not describe the underlying tracer kinetics, bias in the kinetic parameters is observed. This can be solved, for example, by adapting the kinetic model for every region in the body (Matthews *et al* 2012), or by limiting the model fitting to only the region of interest in which the model is accurate (Angelis *et al* 2019).

Another method used to reduce noise in dynamic PET reconstruction is the kernel method (Wang and Qi 2015, Wang 2019). This method regularizes noise in the image domain by incorporating prior information for every voxel in the reconstruction calculation. By using voxel features calculated from image reconstructions with lower noise, correlation between voxels is calculated to construct a spatial kernel matrix. This matrix is multiplied with a scale vector to calculate every dynamic frame. Using the maximum-likelihood expectation-maximization (EM) algorithm the scale vector coefficients of this kernel matrix can be iteratively calculated. A temporal kernel matrix can be used together with the spatial kernel matrix to also consider correlation between time frames for noise reduction. This approach has been implemented using temporal spectral basis functions (Novosad and Reader 2016), or temporal basis functions calculated from correlations in the frames projection data (Wang 2019). The former approach requires knowledge, or estimation, of the input/generating function. For the latter approach no kinetic model is assumed and the temporal basis functions are calculated to cover a finite neighbor around each frame. This approach is useful when no knowledge of the underlying tracer kinetics is known.

It is important to note that most of dynamic PET reconstruction methods have been validated for human studies. Implementing these methods in mouse brain studies can present some differences compared to human studies. For example, the kernel reconstruction method relies on structural similarity among voxels. However, due to the lower relative resolution in mouse brain, individual brain regions span only a few voxels in mouse brain PET images, whereas the analog human brain regions typically span a few tens to hundreds of voxels in the PET image.

In this work, we compare different dynamic reconstruction methods for determination of the [^{11}C]raclopride non-displaceable binding potential (BP_{ND}) and R_1 in the mouse striatum at different noise levels, or equivalently, at different injection activities. The simplified reference tissue model (SRTM) is used as kinetic model, which has been validated elsewhere for raclopride in mouse brain studies (Fischer *et al* 2011). We investigated spatiotemporal kernel reconstruction methods (Wang and Qi 2015, Wang 2019), HYPR denoising (Christian *et al* 2010), and direct reconstruction using SRTM (Lammertsma and Hume 1996, Gravel and Reader 2015) for noise reduction in dynamic PET reconstruction. Moreover, we use the HYPR denoising method within the spatial kernel matrix calculation to reduce noise in the voxel feature frames. We compared BP_{ND} and R_1 calculated from reduced counts realizations and full counts data. This will allow us to point a reconstruction method robust enough to perform accurate kinetic modeling using injected activities sufficiently low to hold the receptor occupancy constraint (Hume *et al* 1998).

2. Methods

2.1. Mice brain scans

Scans were performed using the Siemens Inveon microPET scanner (Siemens Medical Solutions, Inc., Knoxville, USA). The scanner consists of 80 rings, with 320 LSO crystals in each ring. The crystal size is 1.51 × 1.51 mm (Bao *et al* 2009).

Ten-months old male mice (C57Bl6/J, Jackson Laboratories) ($n = 11$) were initially anesthetized using isoflurane anesthesia (5% for induction, 1.5% for maintenance). Animals were then positioned in the scanner bed syde-by-syde (2 mice per scan), with temperature controlled using a heating pad, and constant monitoring

of respiratory rate (Minerve, France). A bolus injection through the tail vein (200 μl) of [^{11}C]raclopride (8.29 $\pm$ 1.65 MBq) was administered using an automatic injection pump with a flow of 1 ml min^{-1}. The injected mass was kept below 4.5 nmol kg^{-1} in order to obtain reliable SRTM BP_{nd} values (Fischer *et al* 2011). Animals were scanned during 60 min, followed by a CT scan to obtain an anatomical image for attenuation correction and image processing. All experiments followed European Committee Guidelines (decree 2010/63/CEE) and the Animal Welfare Act (7 USC 2131), approved by the Ethical Committee for Animal Testing (ECD 2018-37) at the University of Antwerp (Belgium).

To study the performance of the different reconstruction methods, realizations with 4, 8, 12, 16 and 32 times less counts as the original data, were calculated by taking interleaving events from the list-mode data. These realizations are referred as r4, r8, r12, r16 and r32 respectively. This was equivalent to an average injected activity of 2.07 (range 1.63–2.71 MBq), 1.04 (0.81–1.35), 0.691 (0.54–0.90), 0.518 (0.41–0.68), and 0.260 (0.21–0.34) MBq. The data with reduced counts was compared with the full counts data (see section 2.4) using all reconstruction methods.

2.2. Reconstruction methods

All reconstructions were performed in a voxel grid of 128 $\times$ 128 $\times$ 159, with a voxel size of 0.776 $\times$ 0.776 $\times$ 0.796 mm in the x, y and z directions respectively. The dynamic reconstruction framing was (no. of frames $\times$ time of each frame): 12 $\times$ 10 s, 3 $\times$ 20 s, 3 $\times$ 30 s, 3 $\times$ 60 s, 3 $\times$ 150 s, 9 $\times$ 300 s.

Independent frame reconstruction (IFR) consisted of ordered subsets list-mode expectation maximization reconstruction, considering 8 subsets and 16 iterations, without scatter nor randoms correction. Attenuation correction was calculated by precorrection of lines of response using the mu-map calculated from the CT image:

$$\boldsymbol{\lambda}^{i+1} = \frac{\boldsymbol{\lambda}^{i}}{\mathbf{P}'\mathbf{W}\mathbf{1}_L}\mathbf{C}^{i}$$

$$\mathbf{C}^{i} = \sum_{l\in\mathscr{S}_m} p_{lj}\frac{1/A_l}{\sum_{j=1}^{J} p_{lj}\lambda_j^{i}},$$

where $[\ ]'$ is the transpose operator, $\boldsymbol{\lambda}^{i} = \{\lambda_j^{i}\}$ is the number of events in voxel j ($j = 1 \ldots J$ voxels) at iteration i, $\mathbf{P} = \{p_{lj}\}$ is the probability of detection of an event emitted from voxel j along LOR l, A_l is the attenuation factor for LOR l, $\mathbf{W}$ is the diagonal LOR weight matrix with normalization factors for every possible detectable LOR L, $\mathbf{C}^{i}$ is the correction image, $1_L \in \mathbb{R}^{L\times 1}$ is a vector with only ones, and the detected events are divided in subsets $\mathscr{S}_m$ ($m = 1 \ldots M$ subsets). The projection matrix $\mathbf{P}$ is factorized to consider spatially variant resolution modeling in the image space:

$$\mathbf{P} = \mathbf{X}\mathbf{H},$$

where $\mathbf{X} \in \mathbb{R}^{L\times J}$ is the line integral matrix, and $\mathbf{H} \in \mathbb{R}^{J\times J}$ is a matrix containing the point spread function (PSF) kernels in every column. Spatially variant resolution modeling was performed using an asymmetric Gaussian PSF model, with a PSF kernel size of 5 $\times$ 5 $\times$ 5 voxels (Miranda *et al* 2020).

2.2.1. Kernel reconstruction methods

The kernel method makes use of a spatial kernel matrix $\mathbf{K}_s \in \mathbb{R}^{J\times J}$ to represent all dynamic PET frames $\boldsymbol{\lambda}^{t} \in \mathbb{R}^{J\times 1}$:

$$\boldsymbol{\lambda}^{t} = \mathbf{K}_s\boldsymbol{\alpha}^{t},$$

where $\boldsymbol{\alpha}^{t} \in \mathbb{R}^{J\times 1}$ is the coefficient vector for frame t ($t = 1 \ldots T$ frames). Here, we calculate $\mathbf{K}_s$ as originally proposed (Wang and Qi 2015). Initially, a feature is calculated for every voxel in the PET image and the similarity between features is calculated. The voxel feature is the image intensity of the voxel in three dynamic frames of 20 min. The elements of the spatial kernel matrix are calculated using the radial Gaussian kernel with $\sigma = 1$. Considering a search box of 9 $\times$ 9 $\times$ 9 voxels, the closest 48 neighbors of each voxel feature were calculated. Finally, a threshold of 0.8 in $\mathbf{K}_s$ was considered to improve contrast in small regions (e.g. the striatum). The coefficient vector $\boldsymbol{\alpha}^{t}$ is iteratively calculated using the kernelized EM algorithm:

$$\boldsymbol{\alpha}^{t,i+1} = \frac{\boldsymbol{\alpha}^{t,i}}{\mathbf{K}_s'\mathbf{P}'\mathbf{W}\mathbf{1}_L}\mathbf{K}_s'\mathbf{C}^{t,i},$$

where $\mathbf{C}^{t,i}$ is the correction image for frame t at iteration i, with data divided in subsets $\mathscr{S}_m^{t}$ for every frame t:

$$\mathbf{C}^{t,i} = \sum_{l\in\mathscr{S}_m^{t}} p_{lj}\frac{1/A_l}{\sum_{j=1}^{J} p_{lj}\lambda_j^{t,i}}$$

and $\boldsymbol{\lambda}^{t,i} = \{\lambda_j^{t,i}\}$ is the PET image frame calculated from $\mathbf{K}_s$:

$$\boldsymbol{\lambda}^{t,i} = \mathbf{K}_s \boldsymbol{\alpha}^{t,i}.$$

The kernel matrix can be adapted to also consider a temporal kernel matrix (Novosad and Reader 2016, Wang 2019). Temporal correlation between dynamic frames is exploited to further reduce noise in every frame. Here we follow the approach by Wang (2019) to calculate the temporal kernel matrix $\mathbf{K}_t \in \mathbb{R}^{T\times T}$. Briefly, the sinogram of the frame is used as the frame feature. Then, the elements of $\mathbf{K}_t$ are calculated using the frame features with the radial Gaussian kernel. A time window of 15 frames is used to calculate the Gaussian kernel. The spatiotemporal kernel matrix is then the Kronecker product $(\mathbf{K}_t \otimes \mathbf{K}_s)$. The coefficient vector for this kernel matrix then becomes $\boldsymbol{\alpha}^k \in \mathbb{R}^{JT\times 1}$ and the dynamic image is $\boldsymbol{\lambda}^k = (\mathbf{K}_t \otimes \mathbf{K}_s)\boldsymbol{\alpha}^k$.

We estimate the coefficient vector using the kernelized EM algorithm:

$$\boldsymbol{\alpha}^{k,i+1} = \frac{\boldsymbol{\alpha}^{k,i}}{(\mathbf{K}_t \otimes \mathbf{K}_s)'(\mathbf{I}_T \otimes \mathbf{P})'(\mathbf{I}_T \otimes \mathbf{W})\,1_{LT}}(\mathbf{K}_t \otimes \mathbf{K}_s)'\mathbf{C}^{k,i},$$

where $\mathbf{I}_T \in \mathbb{R}^{T\times T}$ is the identity matrix, $\mathbf{C}^{k,i}$ is the dynamic correction image at iteration i:

$$\mathbf{C}^{k,i} = [\mathbf{C}^{k1,i'}\ \mathbf{C}^{k2,i'}\ \ldots\ \mathbf{C}^{kT,i'}]',$$

where:

$$\mathbf{C}^{kt,i} = \sum_{l\in\mathcal{S}_m^t} p_{lj}\frac{1/A_l}{\sum_{j=1}^{J} p_{lj}\lambda_j^{kt,i}}$$

and $\boldsymbol{\lambda}^{kt,i} = \{\lambda_j^{kt,i}\}$ is the frame t image calculated from the dynamic image $\boldsymbol{\lambda}^{k,i} = [\boldsymbol{\lambda}^{k1,i'}\ \boldsymbol{\lambda}^{k2,i'}\ \ldots\ \boldsymbol{\lambda}^{kT,i'}]'$ using the kernel matrix:

$$\boldsymbol{\lambda}^{k,i} = (\mathbf{K}_t \otimes \mathbf{K}_s)\boldsymbol{\alpha}^{k,i}$$

In practice, we use the property of the Kronecker product:

$$\boldsymbol{\lambda}^k = (\mathbf{K}_t \otimes \mathbf{K}_s)\boldsymbol{\alpha}^k \leftrightarrow \boldsymbol{\Lambda}^k = \mathbf{K}_s\mathbf{A}^k\mathbf{K}_t',$$

where $\boldsymbol{\Lambda}^k \in \mathbb{R}^{J\times T}$ is the dynamic image vector, containing every frame concatenated in every column, and $\mathbf{A}^k \in \mathbb{R}^{J\times T}$ is the coefficient vector concatenated in the same fashion.

2.2.2. Direct reconstruction

Direct reconstruction methods have been proposed to simplify the use of the kinetic model in the dynamic tomographic reconstruction. We implemented here the one-step-late approach proposed by Matthews *et al* (2010) and adapted by Gravel and Reader (2015) to include the SRTM model using basis functions (Gunn *et al* 1997):

$$C_n(t) = \theta_{1n}C_R(t) + \theta_{2n}B_n(t),$$

where $C_R(t)$ is the reference region (cerebellum) TAC, $C_n(t)$ is the n-th tissue ($n = 1 \ldots N$) time activity curve (TAC) calculated from the nth basis function $B_n(t)$:

$$B_n(t) = C_R(t) \star \exp(-\theta_{3n}t)$$

and $\star$ is the convolution operator. In our case $N = 120$, with θ_{3n} chosen from a library of logarithmically spaced values from 5.7 e-4 s^{-1} to 0.017 s^{-1}. The cerebellum TAC was obtained from an IFR, using an MRI template in which the mouse cerebellum was delineated (see section 2.3). Weighted linear least squares fit is performed to calculate θ_{1n} and θ_{2n} for every basis function $B_n(t)$ and parameters using the basis function which gives the best fit are selected. We defined a box enclosing the mouse brain and the fit was performed only for voxels within the box after every subset iteration.

2.2.3. HYPR denoising

The highly constrained back-projection (HYPR) is a post-processing denoising method applied in the image space (Christian *et al* 2010). The composite image of all frames is used to denoise every individual dynamic frame. We used this method, with a $3\times\ 3\times\ 3$ boxcar filter, to denoise the IFR. Moreover, we used HYPR to denoise the 3 frames used as the voxel features to calculate the spatial kernel matrix. This method has been proven to perform better than Gaussian post-filtering (Christian *et al* 2010).

In summary, 7 different methods were compared: IFR, IFR with HYPR denoising (IFR + HYPR), kernel reconstruction using only the spatial kernel matrix (KERS), KERS using HYPR to denoise the voxel feature frames (KERS-HYPR), kernel reconstruction using the spatiotemporal kernel matrix (KERST), KERST using HYPR to denoise the voxel feature frames (KERST-HYPR), and direct reconstruction with the SRTM basis function model (DIR-SRTM).

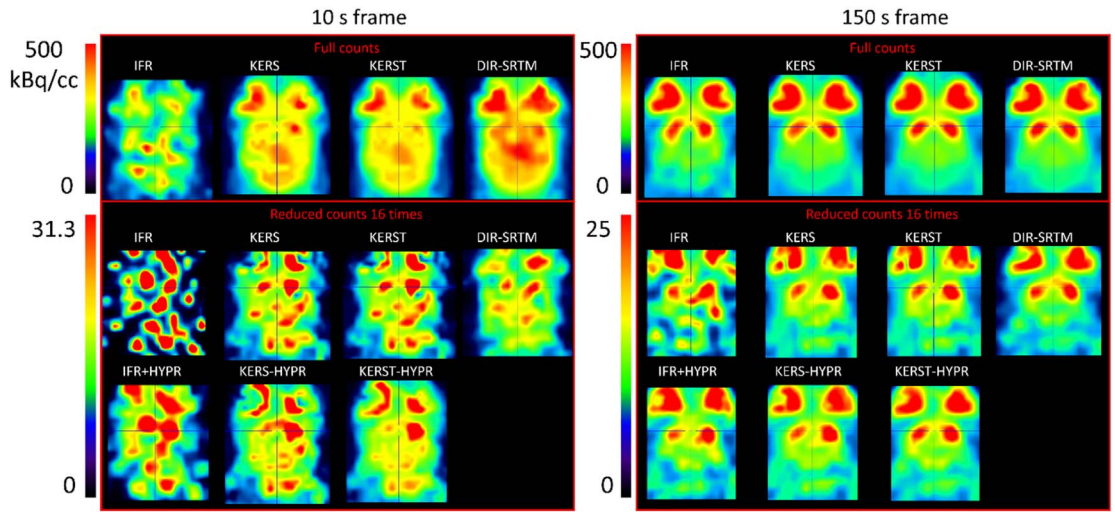

Figure 1. Transverse mouse brain slice of a 10 s (left, 70 s post-injection) and 150 s (right, 450 s post-injection) frame, for the full counts (top row) and reduced counts data with a factor of 16 (middle and bottom row), using all methods.

2.3. Image processing

All dynamic reconstructions were processed in the same manner using the software PMOD 3.6 (Pmod technologies, Zurich, Switzerland). Initially, all dynamic frames were upsampled to a voxel size of 0.22 × 0.22 × 0.22 mm and aligned to the CT image. The head was cropped from the upsampled image and the brain in the CT image was rigidly aligned to and MRI template. The MRI template was created from the average MRI image of 6 age-matched male mice (C57Bl6/J, Jackson Laboratories), in which the whole brain, striatum and cerebellum regions were manually delineated (Bertoglio *et al* 2020). The same rigid registration from CT to MRI was applied to all PET dynamic frames and the striatum and cerebellum TACs were calculated from the template regions (Bertoglio *et al* 2018). The SRTM model was fitted to the striatum TACs, with the cerebellum as reference region, using nonlinear least squares fit. The striatum BP_{ND} and R_1 is reported. Additionally, BP_{ND} and R_1 parametric maps were calculated by fitting the SRTM2 model (Wu and Carson 2002) to all voxels with the k_2' defined with the regional SRTM analysis. The Gpufit library was used to perform the voxel-wise fit (Przybylski *et al* 2017).

2.4. Data analysis

Data analysis was performed in GraphPad Prism 7 (GraphPad Software, California, USA) and Matlab (The MathWorks, Inc., Massachusetts, USA). The correlation in regional striatum BP_{ND} and R_1 between full counts data and reduced counts (r4, r8, r12, r16 and r32) is reported considering all eleven mice. The Bland–Altman method of comparison, i.e. the mean bias and SD in relative difference between full and reduce counts BP_{ND} and R_1 is also performed for regional striatum for all noise realizations. Finally, the average (considering all mice) voxel-wise Pearson's *r* correlation between full counts and reduced counts parametric BP_{ND} and R_1 maps is presented. Reduced counts reconstructions were compared with the respective full counts reconstruction using the same reconstruction method. Only for the methods using HYPR denoising (i.e. IFR, KERS and KERST), the comparison was made with the same full counts reconstruction method but without HYPR denoising, to investigate possible bias introduced by the HYPR denoising.

3. Results

3.1. Image reconstruction, TACs, and BP_{ND}, R_1 parametric maps

Figure 1 shows the reconstruction of a frame of 10 and 150 s using all methods, for the full and reduced counts data with a factor of 16 for a representative mouse. In the full counts data 10 s frame, the reconstruction is improved using KERS, KERST and DIR-SRTM compared to IFR. In the reduced counts image 10 s frame, all methods show high level of noise in the entire brain, but using spatial and/or temporal regularization (i.e. except IFR) a better definition of the brain structure is seen comparable to the full count IFR reconstruction. In the 150 s frame with full counts, all methods show a similar image quality, although IFR displays some deformation in the striatum. In the reduced counts images, among all methods with spatial and/or temporal regularization IFR + HYPR remained the noisiest image while KERST-HYPR shows the most symmetric striatum image.

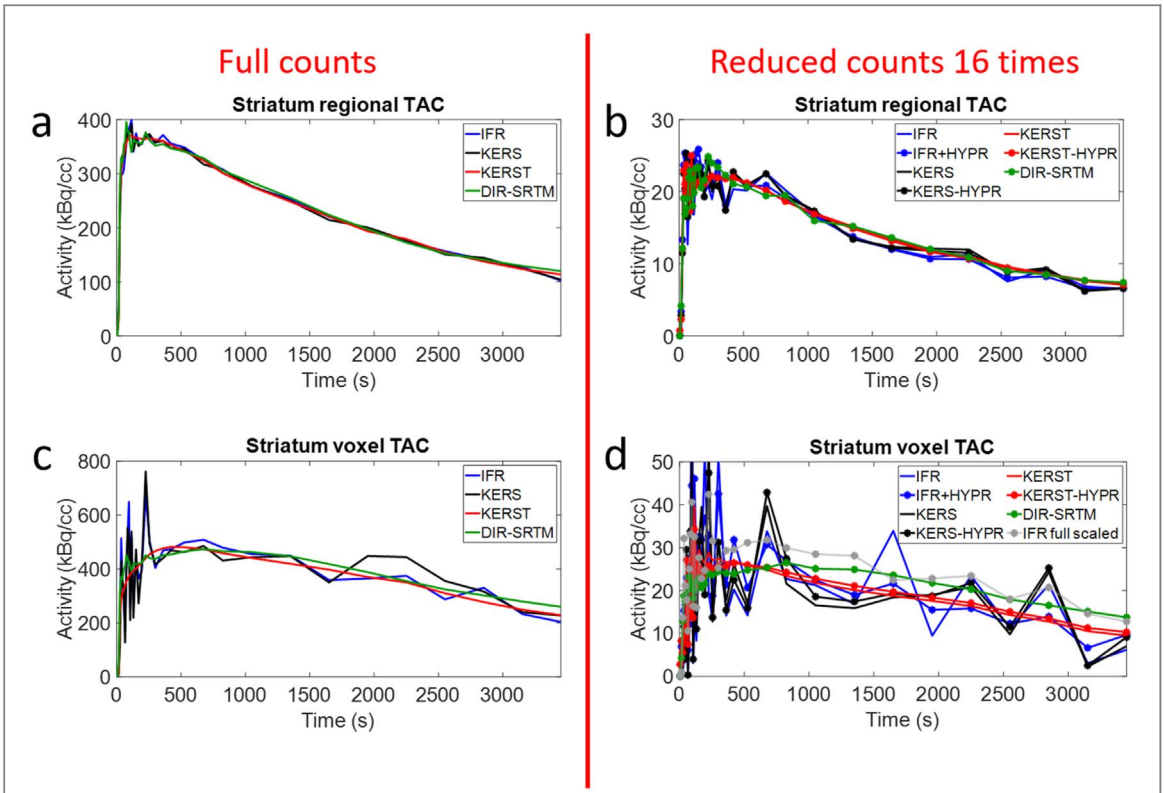

Figure 2. Regional striatum TAC for (a) full and (b) reduced counts data using all methods. TAC for a single voxel within the striatum for (c) full and (d) reduced counts data using all methods. Light-gray TAC in (d) shows the IFR full counts voxel TAC scaled by a factor of 16.

Striatum regional and (one) voxel-wise TACs are shown in figure 2 from a representative mouse, for full and reduced (16 times) counts using all methods. Full counts TACs are very similar amongst all methods, with KERST showing less noise in the short time frames (peak). At the voxel level, the full counts TAC shows high level of noise in the short time frames using IFR and KERS, and is reduced using KERST and DIR-SRTM. In the regional TACs with reduced counts (factor of 16), noise is visible even in the long time frames (tail) using all methods except for KERST, KERST-HYPR and DIR-SRTM. At the single voxel level, noise is high in all frames, but is greatly reduced using the methods with temporal regularization (KERST, KERST-HYPR and DIR-SRTM). For this particular voxel, DIR-SRTM shows good agreement with the full counts IFR TAC at the last frames, although for other voxels discrepancy was similar to the other methods.

Figure 3 shows the brain BP_{ND} parametric maps calculated using all methods, for full and reduced counts data with a factor of 16. Parametric maps calculated from full counts data are similar using all reconstruction methods, showing no artifacts and good symmetry in the striatum BP_{ND}. On the other hand, the parametric maps from r16 using IFR shows asymmetric striatum BP_{ND} and artifacts in other brain regions. Artifacts are reduced using reconstructions with spatial and/or temporal regularization, but asymmetric striatum BP_{ND} is still visible. Striatum shape and symmetry, compared to full counts parametric maps, is improved using the kernel reconstructions with HYPR denoising of the feature frames (KERS-HYPR, KERST-HYPR), and DIR-SRTM.

Figure 4 shows the parametric R_1 maps for all reconstruction methods, in the full and reduced counts data with a factor of 16. Full counts R_1 maps show a uniform distribution throughout the brain for all methods, with IFR showing low intensity non-uniformity in some regions. The reduced counts R_1 maps using IFR are the noisiest, with cold and hot spots throughout the brain. Uniformity is improved using methods with spatial and/or temporal regularization, with DIR-SRTM showing more noise. For the kernel methods, the use of HYPR denoising in the spatial kernel matrix improves homogeneity in the reduced counts R_1 maps, which are also the most homogenous among methods with regularization.

3.2. Regional striatal BP_{ND} and R_1

Table 1 shows the correlation in regional striatum BP_{ND}, as well as linear regression slope and intercept, between full and reduced counts data using all reconstruction methods, for the 5 different levels of counts reduction. The correlation is high using all methods in all noise realizations ($r > 0.94$ in all cases). For r4, IFR and IFR + HYPR show the lowest correlation, 0.991 and 0.980 respectively. For r8, DIR-SRTM shows the lowest correlation

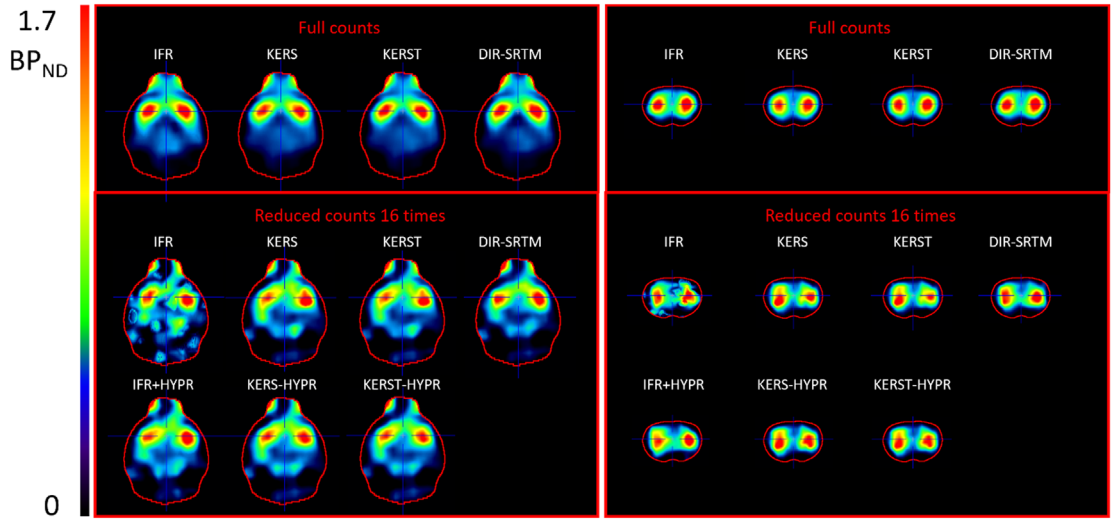

Figure 3. Transverse (left) and coronal (right) slices of the brain BP_{ND} parametric maps calculated from dynamic reconstructions using all methods, for full (top row) and reduced counts data with a factor of 16 (middle and bottom row). Brain outline shown in red.

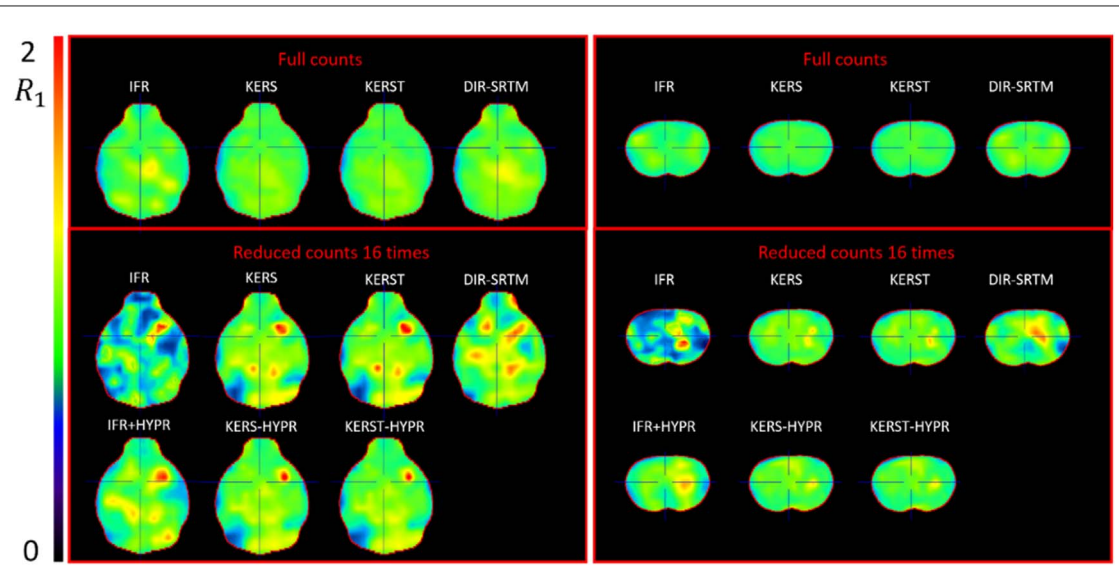

Figure 4. Transverse (left) and coronal (right) slices of the brain R_1 parametric maps calculated from dynamic reconstructions using all methods, for full (top row) and reduced counts data with a factor of 16 (middle and bottom row). Brain outline shown in red.

(0.981), while KERS-HYPR shows the highest correlation (0.992). For r12, IFR shows the lowest correlation (0.970), with IFR + HYPR improving it slightly (0.973), while KERST shows the highest correlation (0.996). For r16, DIR-SRTM shows the lowest correlation (0.975) among the methods with spatial and/or temporal regularization. For r32 KERST-HYPR shows the highest correlation (0.967), while DIR-SRTM shows the smallest (0.942). For all noise realizations, except for r12, the additional HYPR denoising in the spatial kernel matrix improved the correlation in the kernel methods. Individual correlation plots for r16 are shown in supplementary figure 1 (available online at stacks.iop.org/PMB/66/115005/mmedia). For all noise realizations, the kernel methods show the linear regression slope closest to 1, while IFR and IFR + HYPR shows the highest deviation from 1. Similarly, linear regression intercept is closer to zero using kernel methods or DIR-SRTM, while it deviates from zero in a higher degree using IFR and IFR + HYPR for all noise realizations.

Supplementary table 1 shows the correlation in regional striatum R_1, as well as linear regression slope and intercept, between full and reduced counts data using all reconstruction methods, for the 5 different levels of counts reduction. Correlation in R_1 is more affected by noise than BP_{ND}, with the largest r for r4 using KERST (0.841), and the lowest r for r32 using DIR-SRTM (0.12). For all noise levels, the kernel methods show the highest correlation (r4 KERST $r = 0.841$, r8 KERS $r = 640$, r12 KERST $r = 0.759$, r16 KERST-HYPR $r = 0.785$), except for r32, in which IFR show the highest correlation ($r = 0.577$), although with a large

Table 1. Regional striatum (mean from left and right) Pearson's r correlation, linear regression slope, and intercept, in BP_{ND} between full and reduced counts reconstructions using all methods, for the 4 different counts reduction levels. Each correlation value is calculated considering 11 mice (see supplementary figure 1).

Reduction factor		IFR	IFR + HYPR	KERS	KERS-HYPR	KERST	KERST-HYPR	DIR-SRTM
4	*r*	0.991	0.980	0.995	0.996	0.995	0.994	0.995
	slope	0.976	0.899	0.977	0.969	0.973	0.975	1.044
	intercept	0.05	0.142	0.051	0.039	0.055	0.042	−0.08
8	*r*	0.987	0.990	0.989	0.992	0.989	0.991	0.981
	slope	0.939	0.908	0.986	0.959	0.999	0.972	1.044
	intercept	0.111	0.125	0.05	0.066	0.041	0.057	−0.06
12	*r*	0.970	0.973	0.993	0.988	0.996	0.991	0.982
	slope	0.906	0.91	0.967	0.964	1.004	0.994	1.067
	intercept	0.114	0.08	0.061	0.036	0.017	0.006	−0.17
16	*r*	0.968	0.980	0.985	0.994	0.988	0.991	0.975
	slope	0.947	0.885	0.955	0.933	0.987	0.96	1.01
	intercept	0.103	0.181	0.125	0.119	0.086	0.098	−0.042
32	*r*	0.966	0.966	0.944	0.963	0.951	0.967	0.942
	slope	0.919	0.869	0.996	0.985	1.019	0.998	1.023
	intercept	0.14	0.204	0.098	0.083	0.076	0.079	−0.056

deviation from 1 in the linear regression slope (1.763), and large intercept (−0.776). For r32, the second best correlation is shown in KERST-HYPR ($r = 0.543$) with a regression slope close to 1 (1.006). Supplementary figure 3 shows individual R_1 correlation plots for r16.

Figure 5 shows the Bland–Altman bias versus SD plots, comparing full and reduced counts regional BP_{ND}, for all noise realizations and reconstruction methods. Without any regularization (IFR), the SD gradually increase as the noise level increase (SD 3.65%–8.83%). Using HYPR denoising (IFR + HYPR) the SD is reduced for r8, r12 and r16 (SD $<$ 6.75%). However, bias is increased using IFR + HYPR (r4, r8 and r12). DIR-SRTM shows the lowest SD for r4 (3.02%), but for the rest of the noise realizations DIR-SRTM SD is larger than when the kernel methods are used (SD $>$ 5.33%). For r8 and r16, using HYPR with the kernel methods (KERS-HYPR and KERST-HYPR) reduce the SD ($<$ 4.9%), and bias is reduced for all noise realization using KERST-HYPR compared to KERST. For r32 bias is increased for KERS and KERST, but reduced by using HYPR. Considering a threshold of 5% bias and 5% standard deviation (red dotted line in figure 5), only KERST and KERST-HYPR are below these thresholds for noise realizations r4–r16, with KERST-HYPR showing the best performance overall. Individual Bland–Altman plots are shown in supplementary figure 2 for r16.

Supplementary figure 5 shows the equivalent Bland–Altman bias versus SD plots for R_1. A large bias is observed for IFR + HYPR ($>$16%) for all noise levels. In contrast, the rest of the methods have a bias smaller than 5% for r4 and it gradually increases with the noise level. Bland–Altman R_1 SD is similar for all methods, with KERS-HYPR showing the smallest SD for r4 (3.92%) and r8 (6.50%), IFR for r12 (5.56%), KERST-HYPR for r16 (6.84%) and KERS for r32 (10.5%). Supplemental figure 4 shows individual R_1 Bland–Altman plots for r16.

3.3. Brain BP_{ND} and R_1 voxel-wise correlation

Table 2 shows the average voxel-wise correlation between full and reduced counts data BP_{ND} parametric maps, for all reconstruction methods, as well as linear regression slope and intercept. Correlation gradually decreases as the noise level increase using IFR. Spatial and/or temporal regularization clearly improves correlation at all noise levels. Among all methods with regularization, IFR + HYPR shows the lowest correlation in all noise realizations except for r32 (0.977, 0.954, 0.934 and 0.917 for r4, r8, r12 and r16 respectively), while DIR-SRTM shows slightly better correlation (0.980, 0.959, 0.940 and 0.928). For KERS and KERST correlation is improved when HYPR is used for r4, r12 and r16, with the greatest improvement shown in r16 and r32 (KERS: r16 from 0.920 to 0.934, and r32 from 0.847 to 0.879, KERST: r16 from 0.925 to 0.938, and r32 from 0.868 to 0.884). There is no large deviation in the linear regression slope from 1 in all cases (slope $>$ 0.940) and little deviation from zero in the intercept as well (intercept $<$ 0.084).

Supplementary table 2 shows voxel-wise correlation between full and reduced counts data R_1 parametric maps, for all reconstruction methods. For all noise levels KESRT-HYPR shows the largest correlation (r4 0.925, r8 0.866, r12 0.815, r16 0.778), except for r32 where KERS-HYPR shows the largest correlation (0.617). The largest deviation in the slope from 1, and the largest deviation from 0 in the intercept, is found using IFR + HYPR, while other methods perform similarly in these metrics.

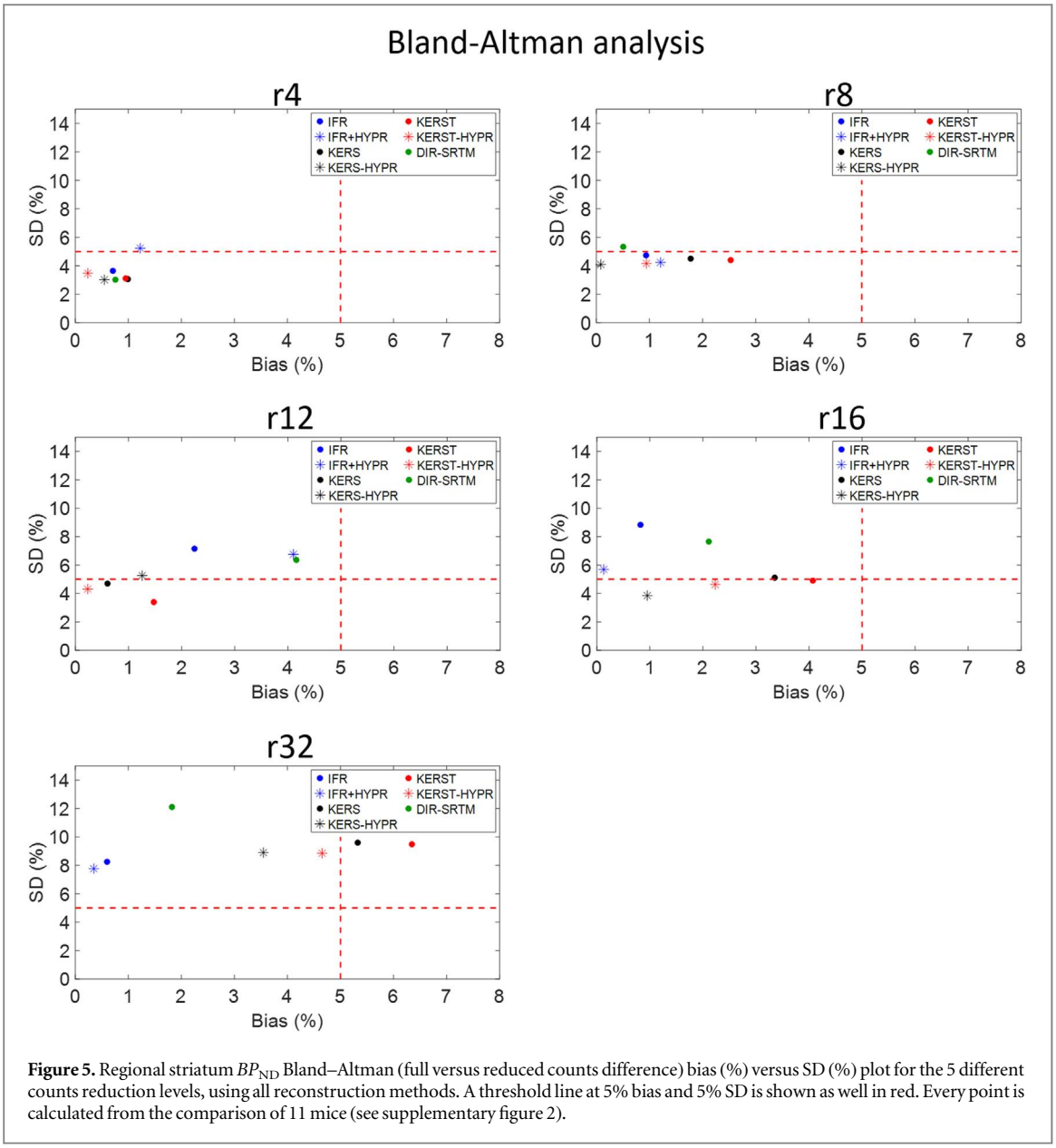

Figure 5. Regional striatum BP_{ND} Bland–Altman (full versus reduced counts difference) bias (%) versus SD (%) plot for the 5 different counts reduction levels, using all reconstruction methods. A threshold line at 5% bias and 5% SD is shown as well in red. Every point is calculated from the comparison of 11 mice (see supplementary figure 2).

Table 2. Voxel-wise average correlation (considering all mice), linear regression slope, and intercept, in BP_{ND} between full and reduced counts parametric maps, using all reconstruction methods.

Reduction factor		IFR	IFR + HYPR	KERS	KERS-HYPR	KERST	KERST-HYPR	DIR-SRTM
4	*r*	0.963	0.977	0.984	0.985	0.984	0.985	0.980
	slope	0.992	0.957	1.007	0.996	1.006	0.996	0.998
	intercept	0.014	0.014	0.000	0.000	−0.001	−0.001	0.003
8	*r*	0.918	0.954	0.961	0.958	0.964	0.963	0.959
	slope	0.982	0.952	1.008	1.000	1.009	0.998	1.006
	intercept	0.028	0.022	0.006	0.006	0.006	0.006	0.017
12	*r*	0.887	0.934	0.943	0.946	0.946	0.948	0.939
	slope	0.969	0.940	1.014	0.998	1.012	1.000	0.981
	intercept	0.029	0.013	−0.003	−0.004	−0.003	−0.004	−0.001
16	*r*	0.844	0.917	0.920	0.935	0.925	0.938	0.928
	slope	0.974	0.958	1.018	0.997	1.019	1.002	0.990
	intercept	0.063	0.031	0.011	0.010	0.009	0.012	0.010
32	*r*	0.733	0.853	0.847	0.879	0.868	0.884	0.844
	slope	0.983	0.958	1.056	1.024	1.053	1.027	1.035
	intercept	0.084	0.029	0.007	0.012	0.013	0.016	0.009

4. Discussion

Kinetic modeling to determine BP_{ND} and R_1 in the mouse brain was investigated using different reconstructions methods, and their robustness to noise was compared. From the quantitative point on view, determining the accuracy of the kinetic modeling parameters in the presence of high noise is equivalent to study their accuracy when the mouse is injected with low activity. Since it has been suggested that tracer activity in the mouse can be restrictively low for the tracer kinetics principle to hold (Hume *et al* 1998), this study will serve to determine which reconstruction methods can allow to obtain accurate results even when extremely low (0.26 MBq) activity is injected in the mouse. Moreover, performance of some of these methods, previously reported only for human studies, is now reported in a small animal study.

Even though the injected dose used in this study most probably caused a receptor occupancy larger than 1%, the injected mass was kept below the limit of 4.5 nmol kg^{-1}, for which a study by Fischer *et al* (2011) showed that SRTM performs with good accuracy. At this limit, receptor occupancy was determined to be around 10%, but still giving good results using SRTM as the kinetic model. Moreover, the statistical accuracy of the SRTM fit to the reference, full counts, data was good enough to consider that, statistically, the model reflects the data correctly (KERST SRTM fit $r^2 > 0.99$, IFR $r^2 > 0.95$).

Qualitatively, post reconstruction spatial denoising using the HYPR algorithm improves the image quality for short time frames. However, using reconstruction methods which perform the regularization within the reconstruction framework, i.e. kernel reconstruction and direct reconstruction methods, produce better image quality. Using both spatial and temporal regularization (KERST, KERST-HYPR) produce reconstructions with better quality (e.g. better striatum uptake symmetry) than using only spatial regularization (KERS, KERS-HYPR) or only temporal regularization (DIR-SRTM).

Regarding the spatial regularization using the spatial kernel matrix, is important to note that the case of mouse brain reconstruction is specially challenging due to the small structures in the brain. Particularly for [^{11}C]raclopride, the dopamine receptors-rich region, the striatum, has a volume of about 10.3×10^{-3} cm^3. Looking at the spatial kernel matrix basis functions for voxels in the striatum, it was observed that, considering the threshold of 0.8, only a couple of voxels (∼1–5) formed the spatial basis functions. In comparison, for voxels in the rest of the brain, spatial basis functions contained the maximum number of voxels (48) in most cases. This could explain why using only kernel spatial regularization, the voxel-wise TACs for striatum still presented a high level of noise. The additional use of temporal regularization in the kernel method can help in the case when the spatial regularization is poor.

Looking at the regional striatum BP_{ND}, correlation between full counts data and noisy data was high ($r > 0.94$) for all noise realizations. Even the IFR showed good results at the regional level ($r > 0.97$), which could be explained by the use of an accurate (experimentally measured) spatially variant PSF in the system matrix (Miranda *et al* 2020). Small differences in the regional BP_{ND} correlation were found between reconstructions considering spatial or temporal regularization (i.e. all methods except IFR). Overall, IFR + HYPR and DIR-SRTM showed slightly lower correlation than the kernel methods, while KERS-HYPR and KERST-HYPR showed the highest correlation. Improvement in the kernel methods using HYPR to denoise the (20 min) frames used to calculate the voxel feature, was observed to a higher degree in the noisiest realization (reduction factor of 32). In this scenario, calculation of the spatial kernel matrix is challenging since the long time frames used as voxel features present themselves a high level of noise. Therefore, correlation between voxels is poor and the spatial kernel matrix basis functions consider less voxels. By using HYPR to denoise the long time feature frames, correlation between voxels is improved and the construction of the spatial kernel matrix basis functions improves.

In the striatum regional BP_{ND} Bland–Altman analysis, a similar trend as in the correlation analysis was observed. IFR + HYPR and DIR-SRTM presented larger SD than the kernel methods up to a noise reduction factor of 16, but bias in some noise realizations was lower for these methods. HYPR denoising in the spatial kernel matrix mostly reduced bias in the kernel methods (KERS and KERST). Again, the largest improvement in bias when using HYPR in the kernel methods was observed in the noisiest realization.

Although we used nonlinear least squares to perform the kinetic modeling, further noise reduction for BP_{ND} at the region level could be obtained using the SRTM basis function approach for kinetic modeling (Gunn *et al* 1997), which, for example, resulted in an increase in correlation for IFR in r16 from 0.968 to 0.985.

At the regional level, R_1 is more affected by noise than BP_{ND}. The largest correlation considering all noise levels and reconstruction methods was 0.84 using KERST. Unlike BP_{ND} at the regional level, performance is markedly different between reconstruction methods. Overall kernel methods show the best correlation, while IFR + HYPR and DIR-SRTM performed worse than IFR in most noise realizations. In the Bland–Altman bias, IFR + HYPR showed large bias compared to the other methods up until r16. Bland–Altman SD was similar for all methods, with the kernel methods showing slightly lower SD overall.

At the voxel level, the correlation in BP_{ND} between full counts and reduced counts reconstructions was decreased to a higher degree than at the regional level for the IFR ($r > 0.73$). Reconstructions with spatial and/or temporal regularization improved this correlation ($r > 0.85$). IFR + HYPR show the least improvement overall, followed by DIR-SRTM. The kernel methods again showed improved correlation when HYPR denoising was used in the spatial kernel matrix feature frames ($r > 0.88$), specially for the realization with most noise. Difference between KERS-HYPR and KERST-HYPR was minimal, i.e. additional temporal regularization in the kernel matrix improved minimally the correlation. Noise reduction using the kernel spatial regularization could be enough for the SRTM model fitting to produce consistent parameters, a model in which BP_{ND} has been shown to be robust in the presence of noise (Gunn *et al* 1997). Kinetic modeling using other less robust or noise-sensitive kinetic models might benefit more by the additional temporal kernel regularization.

Similar to the regional level, correlation at the voxel level for R_1 was more affected by noise. In this case IFR showed the lowest correlation for all noise levels (min–max r, 0.312–0.776), followed by IFR + HYPR (0.545–0.814) and DIR-SRTM (0.534–0.862). The spatiotemporal kernel method with HYPR denoising of the spatial kernel matrix features, showed the best performance overall at the voxel level, with the minimum and maximum correlation in r32 (0.615) and r4 (0.925) respectively.

Regarding the use of only temporal regularization using DIR-SRTM, although its performance was always better than IFR in BP_{ND} calculation, kernel spatial regularization (KERS or KERS-HYPR) performed better. At a low noise level (r4) DIR-SRTM perform similar to the kernel methods, but at higher noise level (r8, r12, r16 and r32) performance was inferior (lower correlation, higher Bland–Altman SD). Noise in the spatial domain could be too high, causing the temporal SRTM fitting to perform suboptimally, producing biased TACs compared to the noiseless TACs. Therefore, spatial regularization seems to be of importance for noise reduction in dynamic PET reconstruction.

As for the temporal regularization in the kernel method, the temporal basis functions used in the temporal kernel matrix are designed to adapt to the data (Wang 2019), and no predefined kinetic model during reconstruction is assumed, as with DIR-SRTM. Therefore, the kernel temporal basis functions allow flexibility to adapt more robustly to the temporal noise. This is particularly beneficial when the kinetic model is not known, or, for example, it can potentially also improve kinetic modeling using an image derived input function, as indicated by our own preliminary data for other tracers (unpublished data). However, the kinetic model needs to be carefully assessed for the specific tracer.

Overall, the spatiotemporal kernel reconstruction with HYPR denoising of the spatial kernel feature frames was the most robust method. It allows to obtain accurate regional BP_{ND} (Bland–Altman bias $< 5\%$, SD $< 10\%$) using SRTM, at injection activities as low as 0.260 MBq, as well as good voxel-wise values (noisy versus full counts data correlation $r > 0.88$) at the same noise level. Performance in R_1 calculation was also the best using KERST-HYPR, but with larger noise than BP_{ND} values. The lowest activity level investigated is close to the 0.3 MBq proposed by Hume *et al* (1998) to achieve a receptor occupancy of 1% using [^{11}C]raclopride with a molar activity of 100 MBq nmol^{-1}. This would allow to perform studies in the mouse brain using [^{11}C]raclopride without compromising the tracer kinetics principle (Fischer *et al* 2011).

5. Conclusions

Several reconstruction methods with spatial and/or temporal regularization were investigated to perform kinetic modeling in the mouse brain in the presence of high noise, or equivalently when the mouse is injected with low tracer activity. HYPR denoising, direct reconstruction with SRTM model, and spatiotemporal kernel reconstruction were investigated in [^{11}C]raclopride using SRTM as the kinetic model. Considering all methods, the spatiotemporal kernel method showed the best performance in terms of correlation and Bland–Altman bias and SD in BP_{ND} and R_1 calculated from full counts data and data with a counts reduction factor of 32, both at the regional and voxel level. Using this reconstruction method, studies with lower injected activity in the mouse can be performed, therefore ensuring the tracer kinetics principle can be maintained.

ORCID iDs

Alan Miranda https://orcid.org/0000-0002-5381-015X
Daniele Bertoglio https://orcid.org/0000-0003-4205-5432

References

Angelis G I, Gillam J E, Ryder W J, Fulton R R and Meikle S R 2019 Direct estimation of voxel-wise neurotransmitter response maps from dynamic PET data *IEEE Trans. Med. Imaging* **38** 1371–83

Bao Q, Newport D, Chen M, Stout D B and Chatziioannou A F 2009 Performance evaluation of the inveon dedicated PET preclinical tomograph based on the NEMA NU-4 standards *J. Nucl. Med.* **50** 401–8

Bertoglio D, Verhaeghe J, Kosten L, Thomae D, Van der Linden A, Stroobants S, Wityak J, Dominguez C, Mrzljak L and Staelens S 2018 MR-based spatial normalization improves [18F]MNI-659 PET regional quantification and detectability of disease effect in the Q175 mouse model of Huntington's disease *PLoS One* **13** e0206613

Bertoglio D, Verhaeghe J, Miranda A, Wyffels L, Stroobants S, Dominguez C, Munoz-Sanjuan I, Skinbjerg M, Liu L and Staelens S 2020 Kinetic modelling and test-retest reproducibility for the dopamine D1R radioligand [(11)C]SCH23390 in healthy and diseased mice *Mol. Imaging Biol.* **23** 208–19

Christian B T, Vandehey N T, Floberg J M and Mistretta C A 2010 Dynamic PET denoising with HYPR processing *J. Nucl. Med.* **51** 1147–54

Fischer K, Sossi V, Schmid A, Thunemann M, Maier F C, Judenhofer M S, Mannheim J G, Reischl G and Pichler B J 2011 Noninvasive nuclear imaging enables the *in vivo* quantification of striatal dopamine receptor expression and raclopride affinity in mice *J. Nucl. Med.* **52** 1133–41

Gravel P and Reader A J 2015 Direct 4D PET MLEM reconstruction of parametric images using the simplified reference tissue model with the basis function method for [(1)(1)C]raclopride *Phys. Med. Biol.* **60** 4533–449

Gunn R N, Lammertsma A A, Hume S P and Cunningham V J 1997 Parametric imaging of ligand-receptor binding in PET using a simplified reference region model *Neuroimage* **6** 279–87

Hume S P, Gunn R N and Jones T 1998 Pharmacological constraints associated with positron emission tomographic scanning of small laboratory animals *Eur. J. Nucl. Med.* **25** 173–6

Innis R B *et al* 2007 Consensus nomenclature for *in vivo* imaging of reversibly binding radioligands *J. Cereb. Blood Flow Metab.* **27** 1533–9

Lammertsma A A and Hume S P 1996 Simplified reference tissue model for PET receptor studies *Neuroimage* **4** 153–8

Matthews J C, Angelis G I, Kotasidis F A, Markiewicz P J and Reader A J 2010 Direct reconstruction of parametric images using any spatiotemporal 4D image based model and maximum likelihood expectation maximisation *IEEE Nucl. Sci. Symp & Med Imaging Conference* **2010** 2435–41

Matthews J C, Reader A J, Angelis G I, Price P M, Markiewicz P J and Kotasidis F A 2012 Adaptive parametric kinetic modelling for improved full field of view fitting of PET data *IEEE Nucl. Sci. Symp and Med Imaging Conf. Record (Nss/Mic)* **2012** 3925–9

Miranda A, Bertoglio D, Glorie D, Stroobants S, Staelens S and Verhaeghe J 2020 Validation of a spatially variant resolution model for small animal brain PET studies *Biomed. Phys. Eng. Express* **6** 045001

Novosad P and Reader A J 2016 MR-guided dynamic PET reconstruction with the kernel method and spectral temporal basis functions *Phys. Med. Biol.* **61** 4624–45

Przybylski A, Thiel B, Keller-Findeisen J, Stock B and Bates M 2017 Gpufit: an open-source toolkit for GPU-accelerated curve fitting *Sci. Rep.* **7** 15722

Reader A J and Verhaeghe J 2014 4D image reconstruction for emission tomography *Phys. Med. Biol.* **59** R371–418

Wang G, Rahmim A and Gunn R N 2020 PET parametric imaging: past, present, and future *IEEE Trans. Radiat. Plasma Med. Sci.* **4** 663–75

Wang G B 2019 High temporal-resolution dynamic PET image reconstruction using a new spatiotemporal Kernel method *IEEE Trans Med. Imaging* **38** 664–74

Wang G B and Qi J Y 2015 PET image reconstruction using Kernel method *IEEE Trans. Med. Imaging* **34** 61–71

Wu Y and Carson R E 2002 Noise reduction in the simplified reference tissue model for neuroreceptor functional imaging *J. Cereb. Blood Flow Metab.* **22** 1440–52